

Equilibration in the time-dependent Hartree-Fock approach probed with the Wigner distribution function

N. Loeb1, J.A. Maruhn1, and P.-G. Reinhard2

¹*Institut fuer Theoretische Physik, Universitaet Frankfurt, D-60438 Frankfurt, Germany and*
²*Institut fuer Theoretische Physik II, Universitaet Erlangen-Nuernberg, D-91058 Erlangen, Germany*

(Dated: November 14, 2018)

Calculating the Wigner distribution function in the reaction plane, we are able to probe the phase-space behavior in time-dependent Hartree-Fock during a heavy-ion collision. We compare the Wigner distribution function with the smoothed Husimi distribution function. Observables are defined to give a quantitative measure for local and global equilibration. We present different reaction scenarios by analyzing central and non-central $^{16}\text{O}+^{16}\text{O}$ and $^{96}\text{Zr}+^{132}\text{Zn}$ collisions. It is shown that the initial phase-space volumes of the fragments barely merge. The mean values of the observables are conserved in fusion reactions and indicate a "memory effect" in time-dependent Hartree-Fock. We observe strong dissipation but no evidence for complete equilibration.

PACS numbers: 21.60.-n, 21.60.Jz

I. INTRODUCTION

The time-dependent Hartree-Fock (TDHF) method was originally proposed as early as 1930 by Dirac [1]. For a long time, it was merely a formal tool to derive many-body approaches like, e.g., in [2] to derive linear response theory. The enormous progress of computational facilities has made TDHF a practical scheme for describing the dynamics of many-body systems. By now it has found widespread applications in various areas of physics. Under the label of time-dependent density-functional theory it is used in electronic systems like atoms, molecules, clusters, and solids, see e.g. [3–5]. The earliest practical applications probably appeared in nuclear physics [6], where TDHF is a powerful microscopic approach to simulate various dynamical scenarios in the regime of large-amplitude collective motion, like fusion excitation functions, fission, deep-inelastic scattering, and collective excitations; for early reviews see, e.g., [7–9]. These pioneering applications were still hampered by the computational limitations of their time. With the ongoing growth of computational power, fully three-dimensional TDHF calculations without any symmetry restriction became feasible and so renewed the interest in nuclear TDHF, for a few recent examples of state-of-the-art TDHF calculations in many different processes see [10–15].

The TDHF approach allows the self-consistent quantum-mechanical description of nuclear dynamics on a mean-field level. Self-consistency means an unprejudiced description once a reliable energy functional is given. This explains the versatility of TDHF. It remains, however, an approximation since it is a mean-field theory. TDHF misses dynamical correlation effects stemming from nucleon-nucleon collisions, which contribute to (two-body) dissipation and thermalization. Their inclusion in a fully quantum mechanical treatment has so far only been achieved in homogeneous systems like, e.g., [16, 17]. Including dynamical correlations for finite nuclei is presently still restricted to a semiclassical description [18–20]. On the other hand, it was found that nu-

clear TDHF calculations already include a great deal of (one-body) dissipation if all terms of the functional, particularly the spin-orbit terms, are properly accounted for [21] and if all symmetry restrictions are removed [22]. This dissipation within TDHF does not result from two-particle collisions but from collision of one particle with the boundaries of the moving mean-field potential ("single-particle dissipation" [23]) which randomizes the single-particle states. In a heavy-ion collision, two pictures of single-particle dissipation can be distinguished. The "window" picture describes dissipation of relative momentum via nucleon exchange through a neck while the "wall" picture deals with the dissipation of kinetic energy by reflection of the nucleons at a moving wall [25–27]. The latter results in a net increase of the nucleons' thermal energy provided there is no correlation between the nucleonic and wall motions. However, these are idealized concepts which are not always immediately applicable to realistic heavy-ion collisions [28–30]. Until now it is not understood at a detailed level how rapidly and how strongly equilibration works within the TDHF approach.

A rough global measure of dissipation is given by comparing initial and final kinetic energies of the fragments in a heavy-ion collision [22]. More detailed analysis should look at something like a local momentum distribution. This naturally leads to the concept of a Wigner function which provides a phase-space picture of a quantum state. Originally introduced in [31], it is often used for establishing the connection between quantum and classical physics [32]. The result of such semiclassical limits is a mean-field dynamics in classical phase-space called the Vlasov equation [34] which is widely used in simulating nuclear dynamics [18–20]. In this paper, we want to stay at the fully quantum-mechanical level and employ the Wigner function as a useful observable helping to analyze TDHF dynamics. An early analysis of that kind is found in [24]. The Wigner function has the weakness that it is not positive semidefinite, thus preventing a strict probabilistic interpretation. This defect is cured

by some phase-space smoothing leading to the Husimi function [35, 36], which also turns out to be the better starting point for the semiclassical expansion [33]. We will also briefly address the Husimi function in connection with TDHF results. As the Wigner function is six-dimensional and thus rather difficult to handle, we deduce from it more compact measures of dissipation and equilibration by considering local quantities integrated with some weights over momentum space, e.g., the eccentricity of the momentum space distribution. These observables are complemented by others computed without recurring to the Wigner picture, e.g., the intrinsic excitation energy which is computed from the local kinetic energy density. We will explore these different analyzing tools for two realistic applications, collision of $^{16}\text{O}+^{16}\text{O}$ and $^{96}\text{Zr}+^{132}\text{Sn}$.

The paper is organized as follows: Section II describes briefly the numerical handling of TDHF used in this work. In Section III we present the transformation from the TDHF wave function to the Wigner and Husimi representations. Results for the ground states in static calculations are presented to compare both pictures. Observables are defined in Section IV to allow a quantitative discussion of equilibration. In Section V we show results for dynamical calculations with different nuclei, energies, and impact parameters.

For sake of generality the formal considerations of Section III are presented in n -dimensional coordinate and $2n$ -dimensional phase space. The results in this paper are obtained in the reduced two-dimensional reaction plane (assumed to be the x - z -plane). For clarity we will label the number of coordinate dimensions n of the applied distribution function f with $f^{(n)}$.

II. FORMAL AND NUMERICAL FRAMEWORK

The basis of the TDHF description is a set of occupied single-particle wave functions $\psi_l(\mathbf{r}, t)$ where l labels the states. These wave functions are two-component spinors. The Skyrme mean-field Hamiltonian is computed for given densities and currents in the standard manner [39]. For all calculations reported here we have used the Skyrme parametrization SkI3 [43].

The TDHF equations are solved on a three-dimensional Cartesian coordinate-space grid. Using the fast Fourier transformation (FFT) derivatives can be evaluated very efficiently in Fourier-space. The mesh spacing is $dx = dy = dz = 1$ fm.

The stationary ground states of the initial systems are computed via the damped-gradient iteration algorithm [40, 41]. The initial state is obtained by placing the ground states of the two fragments in a safe distance and giving them a boost towards each other. These states are then propagated in time by use of a Taylor-series expansion of the time-evolution operator [42] where the expansion is taken up to sixth order. The actual time step is $t = 0.2$ fm/c.

III. WIGNER AND HUSIMI DISTRIBUTIONS

The Wigner function is a transformation of the density matrix to a phase-space function. There are various levels of density matrices in a many-body systems and accordingly various Wigner functions. TDHF can be considered as describing the dynamics of the one-body density matrix $\rho(\mathbf{r}, \mathbf{r}')$, neglecting all correlations between the interacting nucleons above the mean-field level. This is related to the one-body Wigner function which is obtained by a partial Fourier transform acting on the relative coordinate $\mathbf{s} = \mathbf{r} - \mathbf{r}'$, i.e.

$$f_W^{(n)}(\mathbf{r}, \mathbf{k}, t) = \int \frac{d^n s}{(2\pi)^n} e^{-i\mathbf{k}\mathbf{s}} \rho\left(\mathbf{r} - \frac{\mathbf{s}}{2}, \mathbf{r} + \frac{\mathbf{s}}{2}, t\right), \quad (1)$$

$$\rho(\mathbf{r}, \mathbf{r}', t) = \sum_l \Psi_l^\dagger(\mathbf{r}, t) \Psi_l(\mathbf{r}', t). \quad (2)$$

Note that these are, in fact, a spin-averaged density matrix and correspondingly a spin-averaged Wigner function. The dimensionality of the transformation is a very compact notation and needs some explanation. Of course, our TDHF calculations are always 3D. The full Wigner function is then a six-dimensional object, obviously a bit bulky. Therefore, we often take cuts and look at the Wigner transformation in reduced dimensions. The notation $f_W^{(1)}$ then means that one coordinate, e.g. x , is transformed from the pair (x, x') in the density matrix to the pair (x, k_x) in the Wigner function. The other two coordinates, y and z in the example, are fixed at a certain value y_0 and z_0 , usually at the center of the nucleus $y_0 = 0$ and $z_0 = 0$. In other words, $f_W^{(1)}(x, k_x)$ denotes $\rho(x, y_0, z_0; x', y_0, z_0; t)$ transformed in the x dimension.

A direct interpretation of the Wigner function as a phase-space probability distribution is not possible because f_W is not positive semidefinite. There can arise situations where the quantum oscillations lead to negative values. These problems are avoided by the Husimi distribution [35, 36]. The Husimi function $f_H(\mathbf{r}, \mathbf{k}, t)$ is obtained by a convolution of the Wigner function with a Gaussian $\mathcal{G}(\mathbf{r}, \mathbf{k})$

$$f_H^{(n)}(\mathbf{r}, \mathbf{k}, t) = \int d^n r' d^n k' \mathcal{G}(\mathbf{r} - \mathbf{r}', \mathbf{k} - \mathbf{k}') \times f_W^{(n)}(\mathbf{r}', \mathbf{k}', t), \quad (3)$$

$$\mathcal{G}^{(n)}(\mathbf{r} - \mathbf{r}', \mathbf{k} - \mathbf{k}') = \frac{1}{\pi^n} e^{-\frac{r^2}{2\Delta r^2}} e^{-\frac{k^2}{2\Delta k^2}}, \quad (4)$$

$$\Delta r \Delta k = \frac{1}{2}. \quad (5)$$

The Gaussian folding averages f_W over the minimal phase-space cell of volume $(2\pi\hbar)^n$ and so successfully wipes out the negative values. On the other hand, it induces some uncertainty which, however, is physical because one cannot localize a particle in phase space better than within a volume of $(2\pi\hbar)^n$. The Husimi folding has one free parameter, the folding width. For best resolution in both directions it should be chosen close to the

width of the wave functions. As a basis for our choice, we use here the nuclear harmonic oscillator model with frequency and width parameter given as

$$\hbar\omega = \frac{41 \text{ MeV}}{A^{1/3}}, \quad \lambda = \frac{m\omega}{\hbar}.$$

This yields the estimate

$$\Delta r^2 = \frac{1}{2\lambda} = \frac{\hbar^2}{2m}\hbar\omega = \frac{A^{1/3} \text{ fm}^2}{2}, \quad (6)$$

$$\Delta k^2 = \frac{1}{4\Delta r^2} = \frac{\lambda}{2} = \frac{1}{2A^{1/3} \text{ fm}^2}. \quad (7)$$

The choice is somewhat ambiguous for nuclear reactions because one could insert the mass number A for the compound system or the average A of projectiles, or fragments respectively. However, these are details which do not hamper the analysis; a good order-of-magnitude guess suffices for the present analysis.

In a first round, we investigate the distributions for nuclear ground states, to understand the basic pattern and to have a benchmark from a case certainly free of excitation. Figure 1 shows slices through static one-dimensional Wigner and Husimi distributions of the ground states for three nuclei, a light, a medium heavy, and a heavy one. The Wigner distributions show marked shell oscillations. The Husimi distributions have efficiently removed these oscillations and represent a smooth curve averaged through the Wigner distributions. The amplitude of the shell oscillations decreases with increasing mass number, but very slowly such that smooth Wigner functions (resembling classical phase-space distributions) are only reached at an order of magnitude $A \approx 5000$ [32, 37]. The Husimi distributions look smooth already for the low mass numbers of really existing nuclei. This, however, is achieved at the price of somewhat blurring the details due to the folding procedure. This is acceptable for the analysis of the distributions as such, i.e. in phase space. It may become misleading when reducing the distributions to compact observables by integrating over phase space or parts thereof, as will be done in Section IV). The Husimi folding may add an offset to such averaged observables. In such a case, the integrations suffice to average out the small-scale oscillations in the Wigner functions. Therefore, we will in the following concentrate our investigations on the use of the Wigner function only.

IV. MORE COMPACT OBSERVABLES

The Wigner and Husimi distributions are illustrative but difficult to handle, being six-dimensional objects. They can be looked at in some selected snapshots and by taking cuts through the 6D phase space. Observables in lower dimensions down to single numbers are necessary complements for the analysis of dynamical processes. In this section, we will introduce local observables which are distributed in 3D coordinate space. They are reduced to single-number observables by further spatial integration.

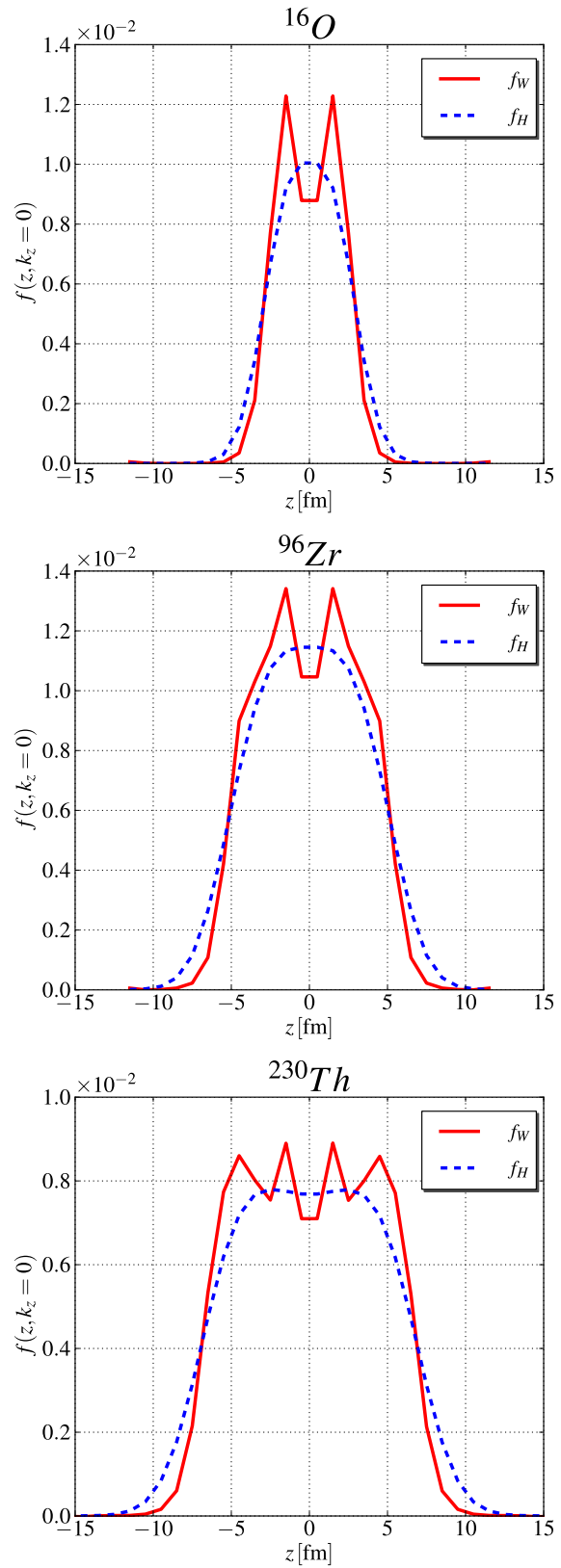


FIG. 1. (color online) Comparison between slices through the one-dimensional Wigner $f_W^{(1)}(z, k_z = 0)$ and Husimi $f_H^{(1)}(z, k_z = 0)$ distribution functions for the static ground states of ^{16}O (top), ^{96}Zr (middle), and ^{230}Th (bottom).

A. Observables from the Wigner distribution

It is a standard procedure in classical non-equilibrium statistical physics to discuss dissipation dynamics in terms of the local momentum distribution, i.e. the momentum distribution at a given space point [45]. The basic features of the local momentum distribution can be characterized by its moments. The first moment

$$\langle \mathbf{k}(\mathbf{r}, t) \rangle_{(n)} = \frac{\int d^n k \mathbf{k} f_W^{(n)}(\mathbf{r}, \mathbf{k}, t)}{\int d^n k f_W^{(n)}(\mathbf{r}, \mathbf{k}, t)}. \quad (8)$$

plays a special role. It characterizes the center of the distribution and it is associated with the average local flow. The higher moments are taken as variances, i.e. relative to the first moment. For the m -th moment this reads

$$\langle \mathbf{k}^{(m)}(\mathbf{r}, t) \rangle_{(n)} = \frac{\int d^n k (\mathbf{k} - \langle \mathbf{k}(\mathbf{r}, t) \rangle)^m f_W^{(n)}(\mathbf{r}, \mathbf{k}, t)}{\int d^n k f_W^{(n)}(\mathbf{r}, \mathbf{k}, t)}. \quad (9)$$

These moments serve as raw material for further reduced observables. Note that they depend on the dimensionality of the Wigner function used in their definition. This is communicated by the index (n) in the moments.

The radial profile of the momentum distribution may be characterized by the ratios of moments, in particular the $m = 4$ to $m = 2$ ratio

$$R^{(n)}(\mathbf{r}, t) = \frac{\langle \mathbf{k}^4(\mathbf{r}, t) \rangle_{(n)}}{\langle \mathbf{k}^2(\mathbf{r}, t) \rangle_{(n)}^2}. \quad (10)$$

Reference value is the thermal equilibrium which corresponds in the high temperature limit to a Maxwellian momentum distribution. These ‘‘equilibrium’’ values are given in Table I for various dimensions.

TABLE I. Analytic values of the ratio $R^{(n)}$ as defined in Eq. (10) for a Gaussian distribution function, depending on the spatial dimension n in which the ratio is evaluated.

dimension n	$R_{\text{gauss}}^{(n)}$
1	3
2	2
3	5/3

The ratios are plagued by the fact that cold equilibrium distributions are Fermi functions rather than Gaussians and, more importantly, are significantly smoothed by quantum effects. This hampers an analysis at a detailed level. A more robust signature of equilibration is obtained by the deformation of the momentum distribution. The leading term is the quadrupole deformation which can be characterized by the eccentricity in the reaction plane, which reads

$$\varepsilon(\mathbf{r}, t) = \frac{\langle k_x^2(\mathbf{r}, t) \rangle - \langle k_z^2(\mathbf{r}, t) \rangle}{\langle k_x^2(\mathbf{r}, t) \rangle + \langle k_z^2(\mathbf{r}, t) \rangle}, \quad (11)$$

where the dimensionality index has been skipped for simplicity. The global eccentricity is obtained by spatial integration

$$\varepsilon(t) = \int dx dz \varepsilon(\mathbf{r}, t) \rho(\mathbf{r}, t), \quad (12)$$

$$\rho(\mathbf{r}) = \int dk_x dk_z f_W^{(2)}(\mathbf{r}, \mathbf{k}, t), \quad (13)$$

with ρ the local density.

B. Intrinsic kinetic energy

Another interesting observable is the intrinsic excitation energy. Ideally, it is defined as the difference between the actual energy and a ‘‘cold’’ reference energy which is obtained from a stationary HF calculation constrained to reproduce the density $\rho(\mathbf{r})$ and current $\mathbf{j}(\mathbf{r})$ of the actual TDHF state [46, 47]. The cumbersome density constrained calculations can be avoided when evaluating the ‘‘cold’’ reference state in Thomas-Fermi approximation. This shortcut was used successfully in Cluster physics [38]. The so approximated intrinsic kinetic energy reads

$$E_{\text{int}}(t) = E_{\text{kin}}(t) - E_{\text{coll,kin}}(t) - E_{\text{TFW}}(t), \quad (14)$$

$$E_{\text{kin}}(t) = \frac{1}{2} \sum_i \int d^3r |\nabla \varphi_i(\mathbf{r}, t)|^2, \quad (15)$$

$$E_{\text{coll,kin}}(t) = \int d^3r \frac{\mathbf{j}^2(\mathbf{r}, t)}{2\rho(\mathbf{r}, t)}, \quad (16)$$

$$E_{\text{TFW}}(t) = \int d^3r \tau_{\text{TFW}}(\mathbf{r}, t), \quad (17)$$

$$\tau_{\text{TFW}}(\mathbf{r}, t) = \frac{3\hbar^2}{10m} (3\pi^2)^{2/3} \rho(\mathbf{r}, t)^{5/3} + \frac{\hbar^2}{18m} \frac{(\nabla \rho(\mathbf{r}, t))^2}{\rho(\mathbf{r}, t)}. \quad (18)$$

It quantifies the non-adiabatic and non-collective component of the kinetic energy, roughly corresponding to the intrinsic thermal energy. The first ingredient for the calculation is the total kinetic energy, E_{kin} , of the system. The second term, $E_{\text{coll,kin}}(t)$, subtracts the hydrodynamic kinetic energy contained in the collective flow \mathbf{j} . The third term, $E_{\text{TFW}}(t)$, subtracts the instantaneous kinetic energy of the zero-temperature ground state at the given density $\rho(\mathbf{r}, t)$. The evaluation of this kinetic energy density $\tau(\mathbf{r}, t)$ is done in the Thomas-Fermi-Weizsäcker approximation [3].

C. An estimate for the fragment distance

As a simple observable characterizing the geometry of a collisional stage, we introduce the distance $d(t)$ between the fragments

$$d(t) = |\langle \mathbf{r}_1(t) \rangle - \langle \mathbf{r}_2(t) \rangle|. \quad (19)$$

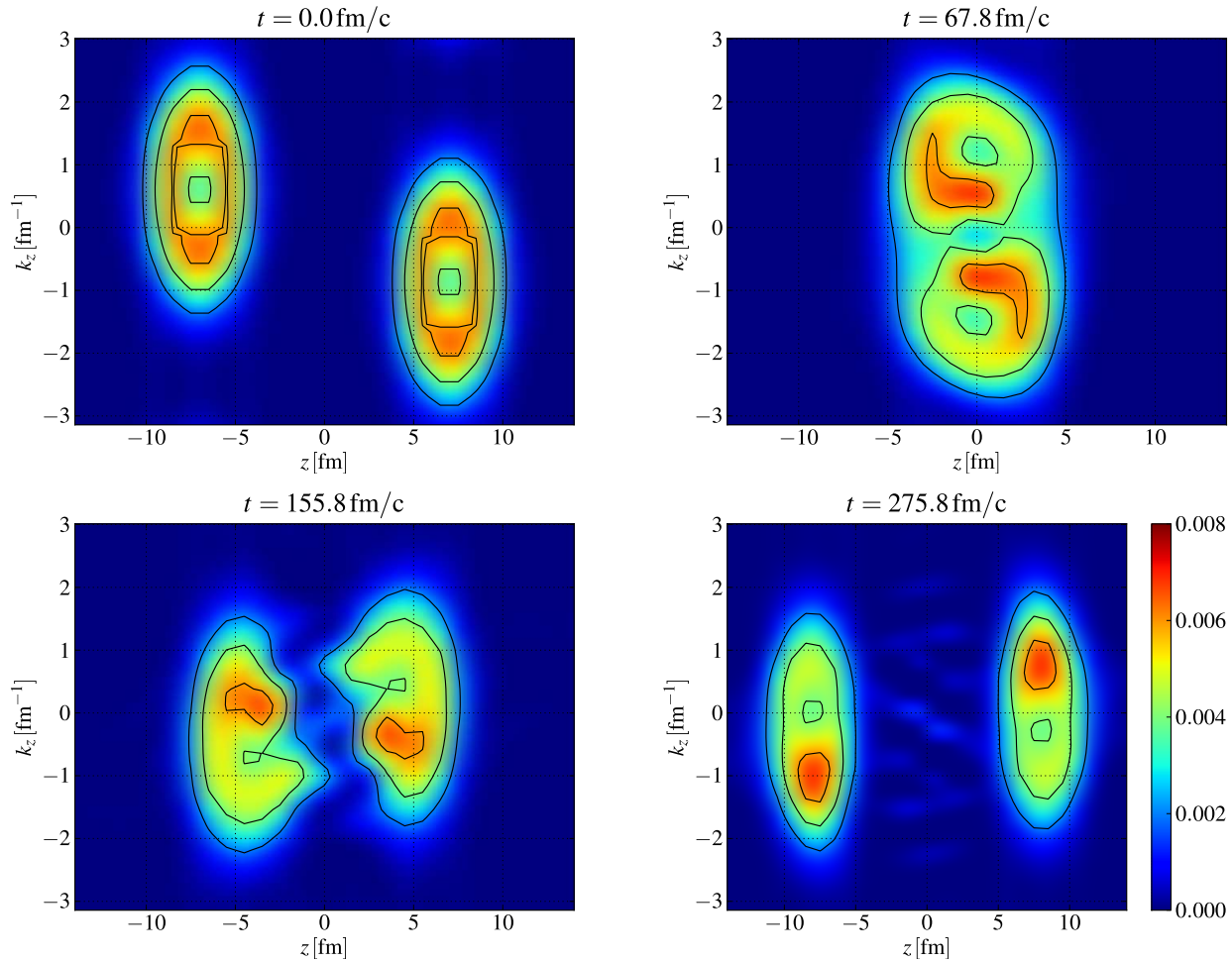


FIG. 2. (color online) The one-dimensional Wigner distribution $f_W^{(1)}(z, k_z, t)$ for a central $^{16}\text{O}+^{16}\text{O}$ collision is plotted at four different times t . Three contour lines are plotted to highlight the levels of $f_W^{(1)}(z, k_z, t)$ at $2 \cdot 10^{-3}$, $4 \cdot 10^{-3}$, and $6 \cdot 10^{-3}$.

The coordinates \mathbf{r}_i of the right and left fragment were obtained by splitting the density of the system symmetrically into two half spaces and averaging over each half. This is an obvious definition for well separated fragments. It becomes somewhat ambiguous in the overlap region, but still remains a useful indicator of the overall geometry.

V. RESULTS

We present TDHF results for different reaction scenarios, $^{16}\text{O}+^{16}\text{O}$ collisions head-on and with finite impact parameter, and a $^{96}\text{Zr}+^{132}\text{Sn}$ collision. The Skyrme parametrization SkI3 [43] is used for the calculations. We performed test calculations with other Skyrme forces and found very similar results. Thus we report the results only from this one force. The central collisions were computed on a coordinate space mesh with 48×24^2 grid points and the non-central ones with 36×24^2 points.

A. $^{16}\text{O}+^{16}\text{O}$ Collisions

1. $^{16}\text{O}+^{16}\text{O}$ Central

First, we analyze a $^{16}\text{O}+^{16}\text{O}$ collision with a center-of-mass energy of $E_{c.m.} = 100$ MeV and zero impact parameter $b = 0$ fm. Figure 2 shows the one-dimensional Wigner distribution $f_W^{(1)}(z, k_z, t)$ at four different stages of the collision. Initially ($t = 0.0$ fm/c), there are two cold nuclei far apart from each other. They are shifted in k_z -direction depending on their initial boost. At the intermediate stage ($t = 67.8$ fm/c), the phase space volumes of the two fragments seem to merge but are avoiding each other, i.e. they maintain a division line. This is a consequence of the Pauli principle. After a while ($t = 155.8$ fm/c), the phase space volumes start to separate, keeping some contact still for some time.

The final stage ($t = 273.8$ fm/c) shows two separate fragments again. But here the structure is quite different as compared to the initial state. Both blobs become

strongly asymmetric. The k_z position of the maximal peaks (red spots) are not lower than initially. But the asymmetry in the distribution extends very much towards lower k_z and also to values of opposite sign. This indicates that the average slowdown in relative c.m. motion in this case is not due to a global downshift of an otherwise symmetric distribution, but to the strong asymmetry reducing significantly the average k_z . A possible interpretation is that the wave functions maintain their initial momentum structure to a large extent but also components from the other fragment are mixed in.

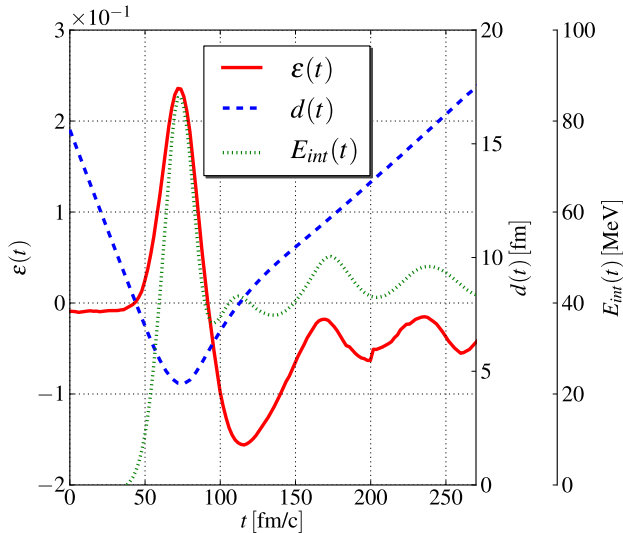


FIG. 3. (color online) The global eccentricity $\varepsilon(t)$ obtained from the two-dimensional Wigner function $f_W^{(2)}(x, z, k_x, k_z, t)$, the distance between the fragments $d(t)$, and the internal kinetic energy $E_{int}(t)$ for a central $^{16}O+^{16}O$ collision with a center-of-mass energy of $E_{c.m.} = 100$ MeV.

In a next step, we analyze the time evolution in terms of compact (single number) observables. The time evolution of the intrinsic kinetic energy $E_{int}(t)$ and of the global eccentricity $\varepsilon(t)$ are shown, together with the fragment distance $d(t)$, in Figure 3. The time of maximum overlap (compound stage) is reached at 75 fm/c where $d(t)$ has a minimum. Both kinetic observables show a pronounced maximum there. As the reaction continues the eccentricity is strongly damped and keeps oscillating at a low level. This indicates some thermalization. The internal energy reaches its maximum at $E_{int} \approx 86$ MeV and saturates, again with some persisting oscillations, at half of the maximal amount. As the potential energy plays a huge role in the compound stage, the values for the kinetic energies have to be taken with care here. The asymptotic values are more directly interpretable. They show significant heating (from $E_{int}(t)$) and great deal of equilibration already within the short time span of the simulation.

To visualize the oscillations in $\varepsilon(t)$ and $E_{int}(t)$ we show in Figure 4 the two-dimensional momentum distribution

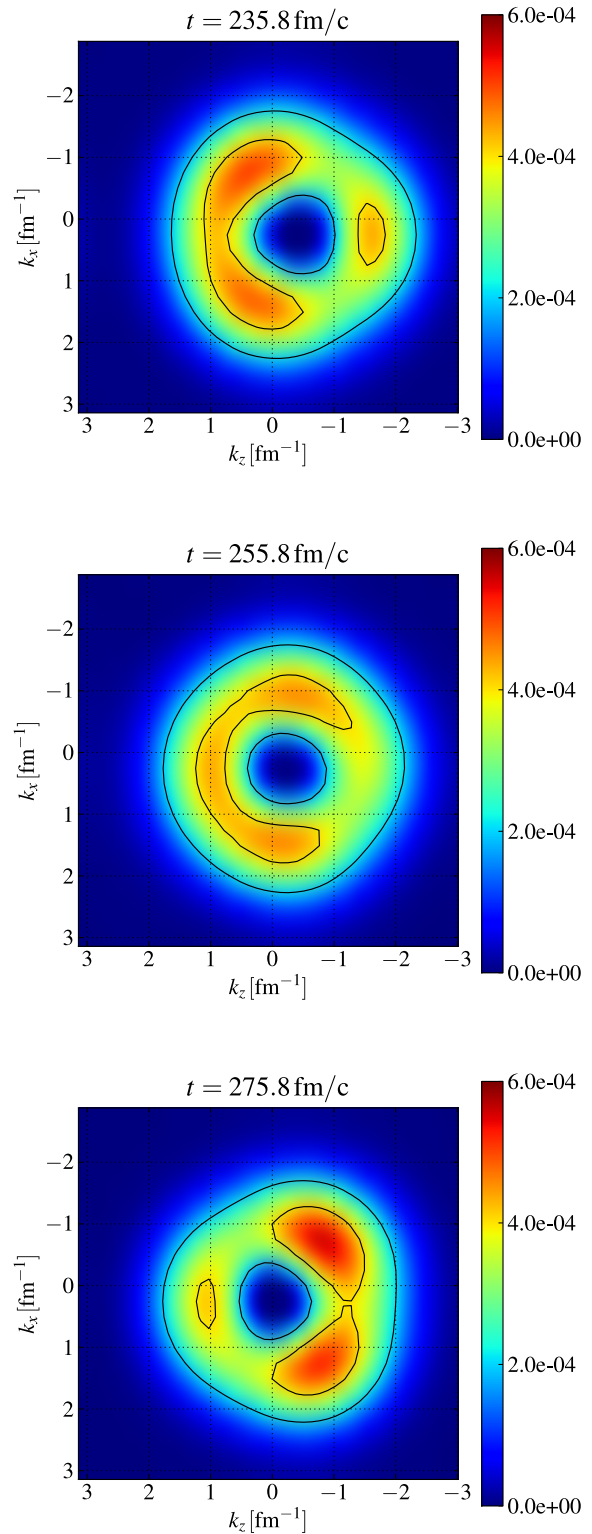


FIG. 4. (color online) A k_x - k_z cut of the two-dimensional momentum distribution $f_W^{(2)}(k_x, k_z, t)$ plotted at the center of the fragment moving finally with negative mean momentum in k_z -direction. The plots are taken at three different times t near the final stage of the calculation. Two contour lines are plotted to highlight the levels of $f_W^{(2)}$ at $2 \cdot 10^{-4}$ and $4 \cdot 10^{-4}$.

$f_W^{(2)}(k_x, k_z, t)$ in the exit channel for the fragment moving to the left (with negative $\langle k_z \rangle$). The shape is asymmetric and oscillates back and forth. This indicates that the largest collective effect in the exit channel is residual octupole oscillations which have their counterpart also in similar octupole oscillations of the fragments' spatial shape.

We have checked the momentum ratio $R^{(n)}(\mathbf{r}, t)$ as given in Eq. (10) for $n = 1, 2$ at different times to probe the closeness of the momentum distribution to a Maxwellian distribution. The comparison with the analytic values R_{gauss} from Tab. I is not conclusive, as quantum effects blur the classical concept behind this ratio by making the distributions too different from Gaussians. This casts some doubts on the usefulness of the global ratio $R(t)$ in this still predominantly quantum-mechanical domain. We will come back to this observable in Section VB.

2. $^{16}\text{O}+^{16}\text{O}$ Non-Central

In this Section we analyze $^{16}\text{O}+^{16}\text{O}$ fusion reactions with non-zero impact parameter $b = 2$ fm and two different center-of-mass energies $E_{c.m.} = 20$ MeV and $E_{c.m.} = 50$ MeV.

Figure 5 shows the global eccentricity $\varepsilon(t)$, the internal kinetic energy $E_{\text{int}}(t)$, and the fragment distance $d(t)$ for both reactions. The distance oscillates after the minimum reached on first impact. This indicates that both cases describe a fused compound state. The eccentricity $\varepsilon(t)$ follows the oscillations of the distance, reflecting a continuing vivid interaction with the spatial deformation. This indicates that we are far from equilibration. The intrinsic kinetic energy grows initially and soon levels off, leaving small residual oscillations about a constant mean value. This mean intrinsic energy is, of course, larger for the higher-energy collision ($E_{c.m.} = 50$ MeV). The example demonstrates nicely that one needs a couple of observables to conclude on equilibration. One may be tempted to take the constant $E_{\text{int}}(t)$ as indicator of a thermalized state. The still large values of eccentricity and the oscillations thereof prove clearly that we are rather in a situation of substantial coherent oscillations of the compound system. In this context, it is to be remembered that the energy stored in the collective motion of the compound system is subtracted in the evaluation of $E_{\text{int}}(t)$.

The demonstrated behavior of the observables was checked up to $t = 4000$ fm/c, twice the time span shown in Figure 5. The pattern carried on unchanged also for these longer times.

B. $^{96}\text{Zr}+^{132}\text{Sn}$

As an example for a much heavier nuclear system we present fusion of $^{96}\text{Zr}+^{132}\text{Sn}$ achieved with a center-of-

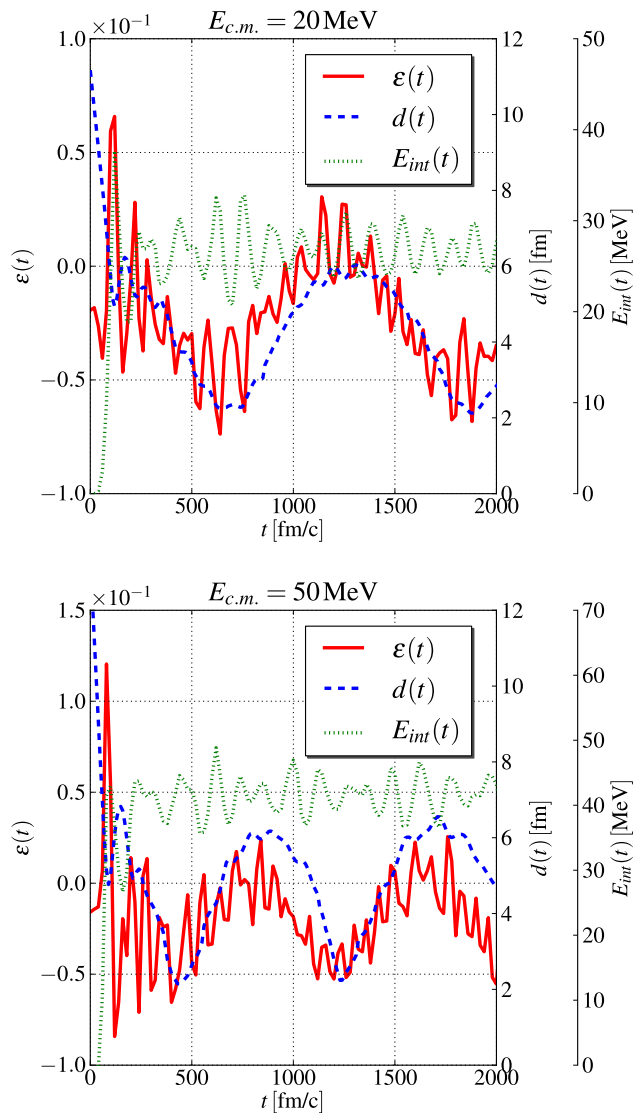


FIG. 5. (color online) The global eccentricity $\varepsilon(t)$ obtained from the two-dimensional Wigner function $f_W^{(2)}(x, z, k_x, k_z, t)$, the distance between the fragments $d(t)$, and the internal kinetic energy $E_{\text{int}}(t)$ for two $^{16}\text{O}+^{16}\text{O}$ fusion reaction with a center-of-mass energy of $E_{c.m.} = 20$ MeV (top) and $E_{c.m.} = 50$ MeV (bottom) and impact parameter $b = 2$ fm.

mass energy of $E_{c.m.} = 250$ MeV and impact parameter $b = 2$ fm. The reaction between the neutron-rich ^{132}Sn nucleus and ^{96}Zr was already studied in TDHF with a focus on barrier heights and widths of the heavy-ion potential as well as capture cross sections [44].

It was not possible in the present analysis to calculate the distance $d(t)$ between the fragments as it was done in the $^{16}\text{O}+^{16}\text{O}$ fusion scenario. The numerical algorithm selecting the spatial expectation values for a two-body system was not able to detect two distinct objects during the whole calculation and in this asymmetric system a simple symmetric division of the grid was not possi-

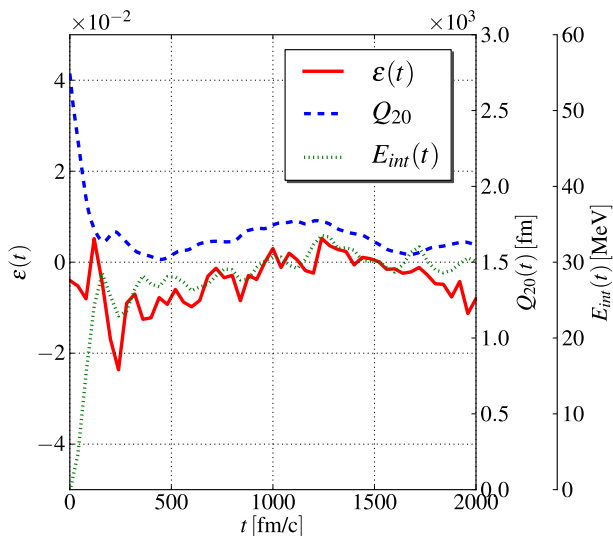


FIG. 6. (color online) The global eccentricity $\varepsilon(t)$ obtained from the two-dimensional Wigner function $f_{\text{W}}^{(2)}(x, z, k_x, k_z, t)$, the quadrupole Q_{20} , and the internal kinetic energy $E_{\text{int}}(t)$ for a $^{96}\text{Zr}+^{132}\text{Sn}$ fusion reaction with a center-of-mass energy of $E_{c.m.} = 250$ MeV and impact parameter $b = 2$ fm.

ble. In Figure 6 we therefore use the expectation value $Q_{20} \equiv \langle \hat{Q}_{20} \rangle$ of the quadrupole operator \hat{Q}_{20} to visualize the global geometry of the reaction. Again, large values indicate separated fragments and low values a compound stage. It is obvious from the figure that the reaction ends in a compound nucleus. The overall trends of intrinsic kinetic energy and eccentricity are to some extent similar to the results in Figure 5. However, the final eccentricity is much smaller, still maintaining some small oscillations. This indicates a better thermalization than seen for $^{16}\text{O}+^{16}\text{O}$, which is no surprise because the single-particle phase space is much larger for the heavier system. The trend of the intrinsic energy does also differ in detail. There seem to be two stages of growth, a fast initial rise on the way to the compound stage and a slower, but steady, growth up to 1000 fm/c. This indicates that some thermalization processes and energy transport from deformation energy to kinetic energy is still going on. After 1000 fm/c we again see a rather constant E_{int} as seems to be typical for energetic compound nuclei.

Figure 7 shows the local ratio $R^{(2)}(\mathbf{r}, t)$ as defined in Eq. (10) in the reaction plane at $t = 1279.8$ fm/c. The surface region is distinguished by large values coming close to the Maxwellian reference values while much smaller ratios are seen inside. In order to illuminate these results, we have a closer look at the more detailed momentum distributions at four selected points indicated in Figure 7. Figure 8 shows results for two the outer points at the surface. The first point (P_1) is taken at approximately half the maximum value of f_{W} . The distribution is very similar to a Gaussian overlaid by a slight asymmetry. The next point (P_2) shows a more pronounced

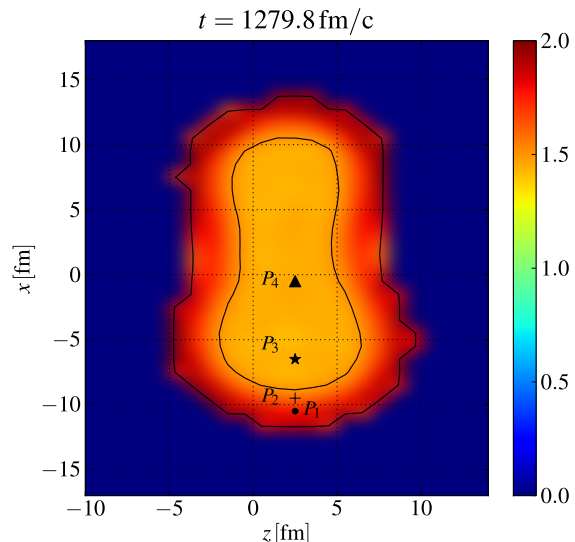


FIG. 7. (color online) The local ratio $R^{(2)}(\mathbf{r})$ obtained from the two-dimensional Wigner distribution $f_{\text{W}}^{(2)}(x, z, k_x, k_z, t)$ for a $^{96}\text{Zr}+^{132}\text{Sn}$ fusion reaction at $t = 1279.8$ fm/c. Four points are marked in this plot to be analyzed later more precisely (Figure 8 and Figure 9). The reference value from a Gaussian distribution is $R_{\text{gauss}}^{(2)} = 2$. A Contour line is plotted to highlight the level of $R^{(2)}(\mathbf{r}) = 1.5$.

asymmetric shape. Moving further to the inner points (P_3, P_4) reviewed in Figure 9 the momentum distributions differ substantially from Gaussians and come closer to the idea of a Fermi distribution, although heavily overlaid by quantum shell oscillations.

An similar analysis of the momentum distribution at other points near the nuclear center yields similar results. The inner region of the merged systems seems to stay rather “cold“ during the reaction.

The strong quantum mechanical shell oscillations hinder a fit of the distribution functions shown in Figure 8 and 9 to a Fermi function from which one eventually could read off an estimate for the system’s temperature distribution. Therefore we compare the $^{96}\text{Zr}+^{132}\text{Sn}$ system to be assumed “hot“ with the “cold“ analogue of this system. Figure 10 shows the momentum distribution of the $^{96}\text{Zr}+^{132}\text{Sn}$ compound system at the point P_4 indicated in Figure 9. This is compared with the result from the prolate ground state of ^{230}Th . The $^{96}\text{Zr}+^{132}\text{Sn}$ system consists of $p = 90$ protons and $n = 138$ neutrons. ^{230}Th shares the same proton number with two additional neutrons. The ground state nucleus shows huge, fully developed shell oscillations. Compared to these, the remaining quantum oscillations in the “hot“ compound state become rather small. The disappearance of quantum shell effects is a major thermalization effect [32, 48]. The occupation of high momentum components, however, which would also be expected for hot systems remains insignificant. This is due to the fact that the nucleus is an open system from which high energy particles

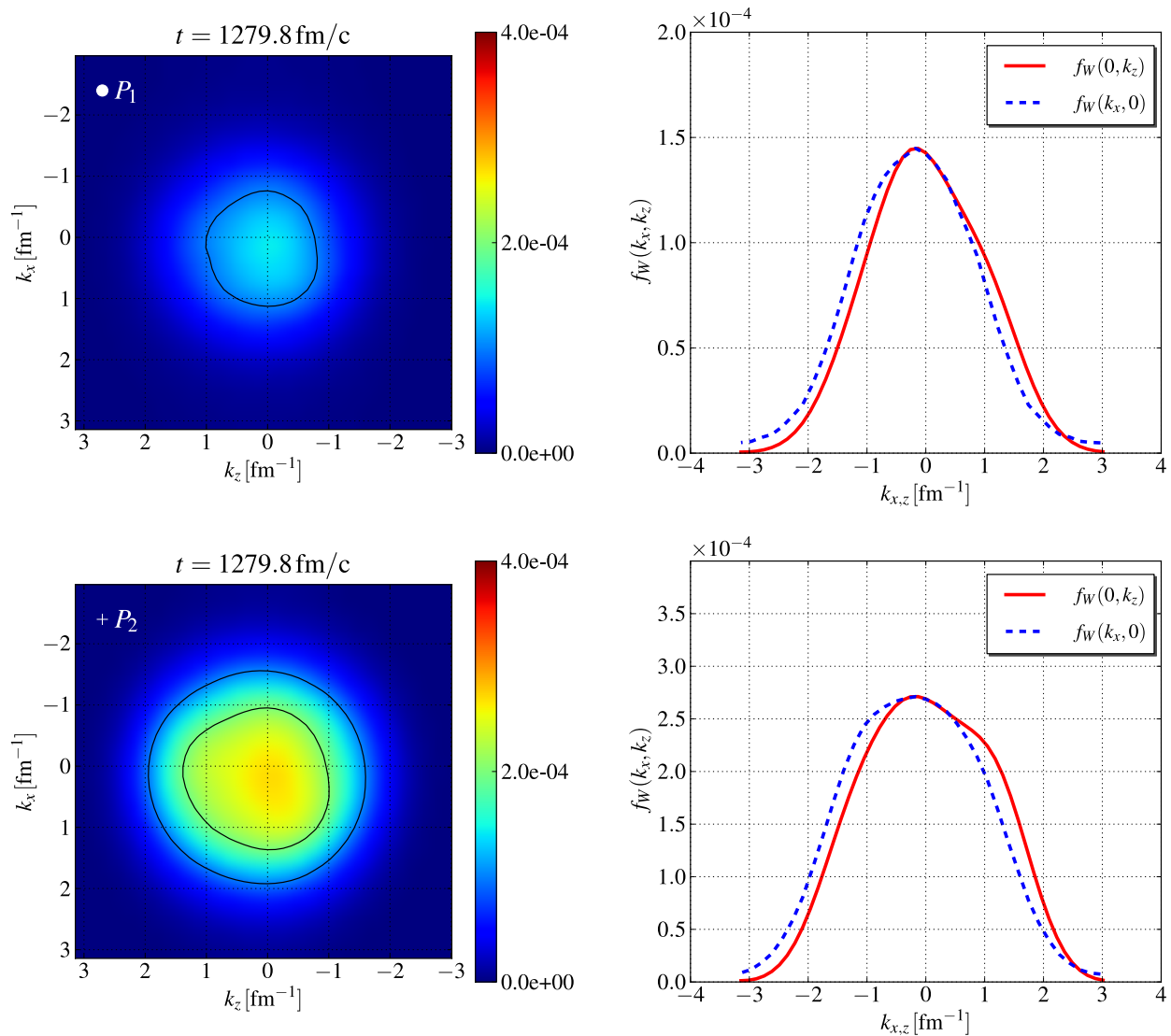


FIG. 8. (color online) The left column reviews the two-dimensional momentum distribution $f_W^{(2)}(k_x, k_z)$ in the selected (outer) points from Figure 7. Contour lines are plotted to highlight the levels of $f_W^{(2)}$ at $1 \cdot 10^{-4}$, $2 \cdot 10^{-4}$, and $3 \cdot 10^{-4}$. Slices through $f_W^{(2)}(k_x, k_z)$ matching the k_x, k_z -axis are shown in the right column.

escape, constantly depleting the high-momentum parts of the distribution. This explains why a fit to Fermi distributions failed. A measure of temperature may be deduced from the suppression of the shell oscillations, but this analysis is blurred by the large thermal fluctuations in the momentum-space density. For the time being, the eccentricity remains the cleanest indicator of equilibration.

VI. SUMMARY

In this work we have analyzed from different perspectives the dynamics of TDHF during various reactions including the nuclei ^{16}O , ^{96}Zr , ^{132}Sn , and ^{230}Th with vari-

ous center-of-mass energies and impact parameters. The key quantity of the analysis is the Wigner distribution function which provides a detailed phase-space picture of the quantum state. As complementing quantities, we also considered three more compact observables in terms of local distributions: the ratio $R(\mathbf{r}, t)$ of the weighted moments (weight four and two) of the local momentum distribution described by the Wigner function (i.e. integrating the Wigner function over momentum space for fixed local position), the eccentricity $\epsilon(\mathbf{r}, t)$ of the local momentum distribution, and the intrinsic excitation energy $E_{\text{intr}}(\mathbf{r}, t)$ as deduced from the kinetic energy density.

General properties of the Wigner distribution were discussed first for stationary states. It shows oscillations

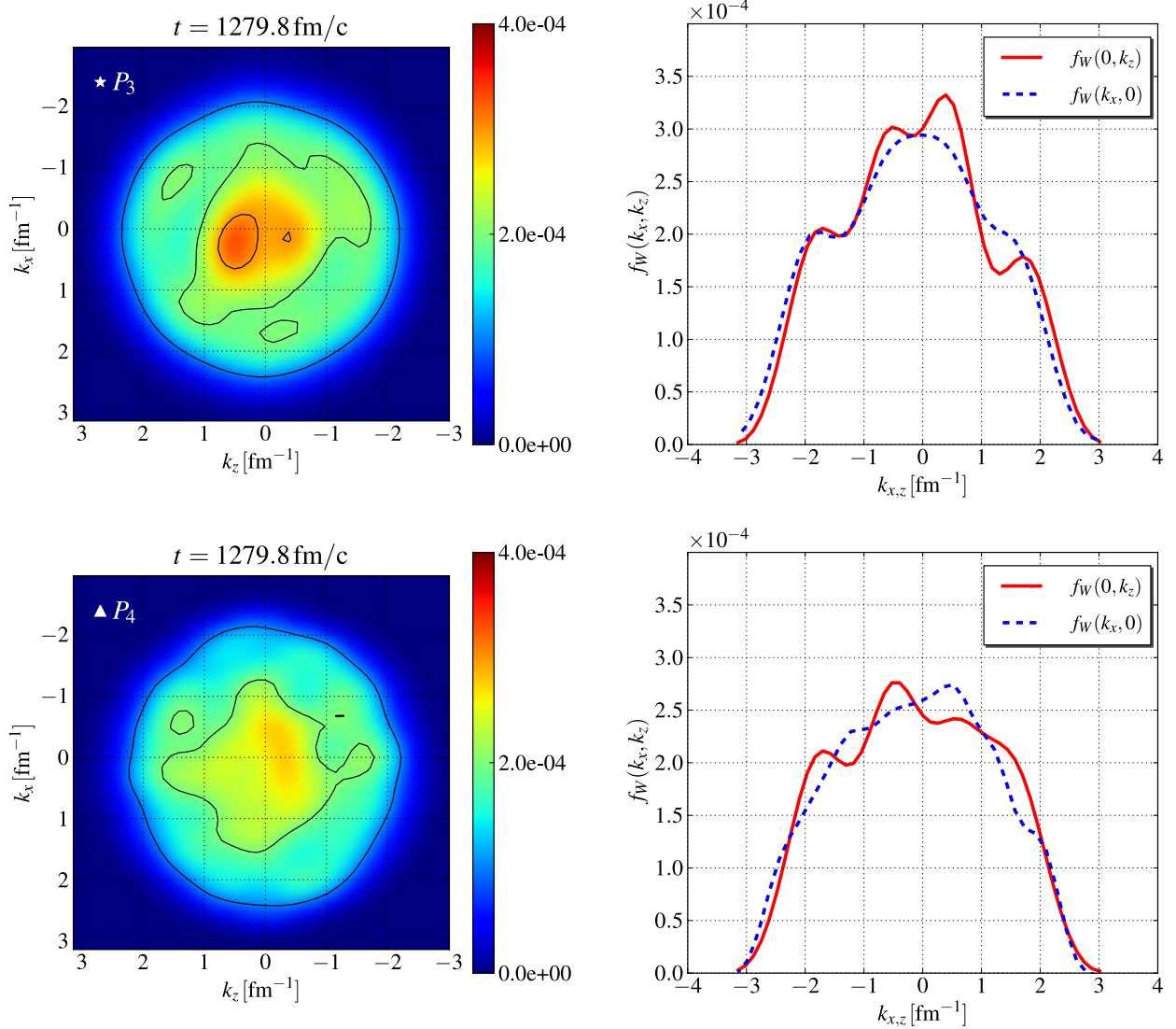
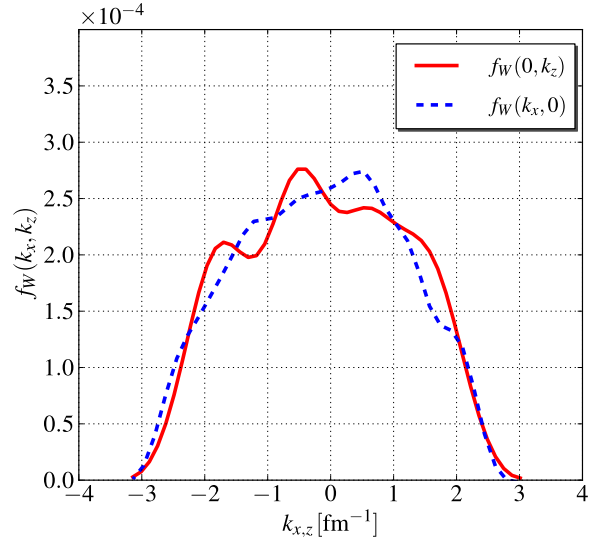
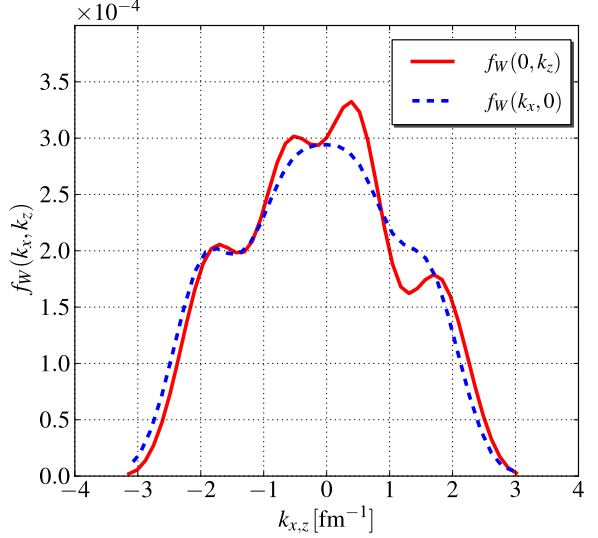


FIG. 9. (color online) Same as Figure 8 but for the selected (inner) points in Figure 7.

which stem from the quantum shell oscillations of the underlying single-particle states. We also looked at the Husimi function derived from the Wigner function by some phase-space smoothing. The latter indeed provides a cleaner and more intuitive picture. We find, however, that the shell oscillations are much reduced in the dynamical scenarios of heavy-ion collisions, allowing us to continue the dynamical studies with the Wigner function alone.

We have visualized the collision process through snapshots of a 2D cut of the 6D Wigner function. This shows that the two initially separated phase space blobs never fully merge, even at the compound stage. The distributions of the emerging fragments acquire a strong asymmetry in momentum space and nicely show the phase space rotations associated with the remaining octupole oscillations of the final fragments.



The moment ratio R was intended as a means to compare the shape of the TDHF-Wigner distribution with a Maxwellian distribution corresponding to thermal equilibrium. We find for all reaction parameters that the moment ratio remains below the Maxwellian reference value, which means that thermalization could not be asserted in this observable. The reason is that the high-momentum tail of the actual distribution is immediately depleted by particle emission. This exemplifies the fact that a true equilibrium state is hard to establish in an open system.

The eccentricity ε turned out to be a more useful indicator. It grows dramatically in the initial phase of the reaction and relaxes to lower values quickly after the compound state and then remains oscillating about some finite value. This means that the final relaxation to a thermal state is probably underestimated in mere TDHF.

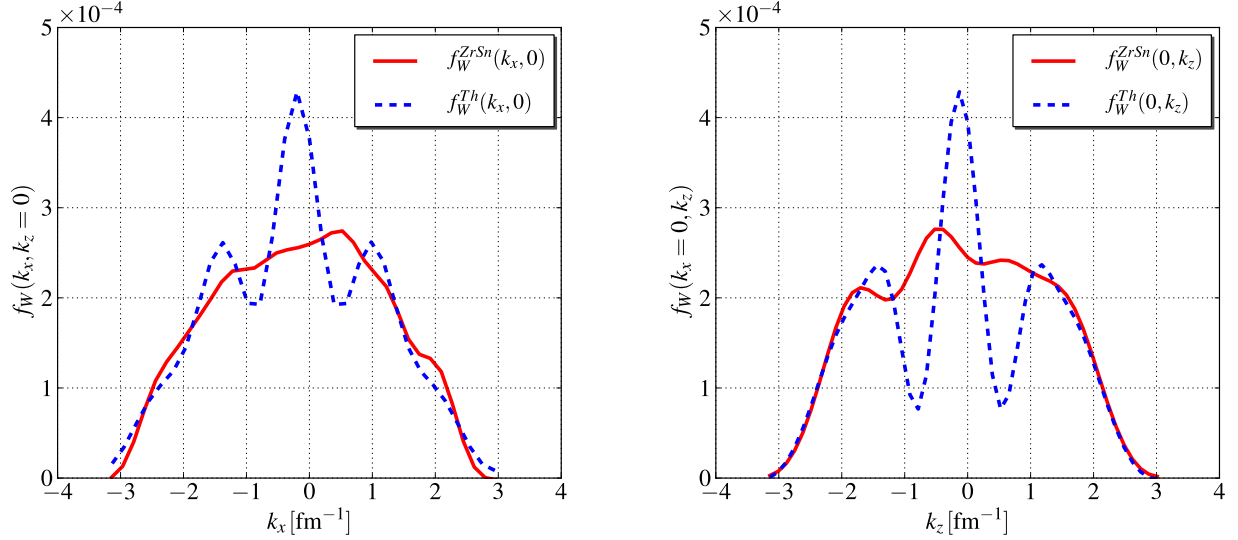


FIG. 10. (color online) Slices along k_x (left) and k_z (right) through $f_W^{(2)}(k_x, k_z)$ are shown for the merged $^{96}\text{Zr}+^{132}\text{Sn}$ system (red) at $t = 1279.8$ fm/c in the point P_4 from Figure 7 in comparison with the ground state of ^{230}Th (blue).

Similar patterns are shown by the intrinsic kinetic energy E_{int} . The resulting “asymptotic” value of E_{int} depends strongly on the initial conditions, e.g., growing with the initial collision energy.

We conclude that although TDHF includes dissipation owing to single-particle viscosity, which acts strongly in the initial phase of reactions, there is no evidence for complete equilibration.

ACKNOWLEDGMENT

This work was supported by the Frankfurt Center for Scientific Computing and by the BMBF under Contracts No. 06FY9086 and 06ER9063. We gratefully acknowledge support by the Frankfurt Center for Scientific Computing.

-
- [1] P. A. M. Dirac, Proc. Camb. Philos. Soc. **26**, 376 (1930).
[2] G. E. Brown, *Unified Theory of Nuclear Models and Forces*, (North-Holland, Amsterdam, 1971).
[3] R.M. Dreizler, E.K.U. Gross, “Density Functional Theory: An Approach to the Quantum Many-Body Problem”, Springer, Berlin, 1990.
[4] P.-G. Reinhard and E. Suraud, *Introduction to Cluster Dynamics* (Wiley, New York, 2003).
[5] *Time-dependent density functional theory*, Vol. 706 of *Lecture Notes in Physics*, edited by M. A. L. Marques, C. A. Ullrich, and F. Nogueira (Springer, Berlin, 2006).
[6] P. Bonche, S. E. Koonin, and J. W. Negele, Phys. Rev. C **13**, 1226 (1976).
[7] J. P. Svenne, Adv. Nucl. Phys. **11**, 179 (1979).
[8] J. W. Negele, Rev. Mod. Phys. **54**, 913 (1982).
[9] K. T. R. Davies, K. R. S. Devi, S. E. Koonin, and M. R. Strayer, in *Treatise on Heavy-Ion Physics*, Vol. 3 Compound System Phenomena, edited by D. A. Bromley (Plenum Press, New York, 1985), p. 3.
[10] K.-H. Kim, T. Otsuka, and P. Bonche, J. Phys. G **23**, 1267 (1997).
[11] C. Simenel and P. Chomaz, Phys. Rev. C **68**, 024302 (2003).
[12] T. Nakatsukasa and K. Yabana, Phys. Rev. C **71**, 024301 (2005).
[13] A. S. Umar and V. E. Oberacker, Phys. Rev. C **71**, 034314 (2005).
[14] J. A. Maruhn, P.-G. Reinhard, P. D. Stevenson, J. R. Stone, and M. R. Strayer, Phys. Rev. C **71**, 064328 (2005).
[15] Lu Guo, P.-G. Reinhard, and J. A. Maruhn, Phys. Rev. C, **77**, 041301 (2008).
[16] C. Toepffer and P.-G. Reinhard, Ann. Phys. **181**, 1 (1988).
[17] C. Greiner, K. Wagner, and P.-G. Reinhard, Phys. Rev. C **49**, 1693 (1994).
[18] G.F. Bertsch, S. Das Gupta, Phys. Rep. **160**, 190 (1988).
[19] A. Bonasera, F. Gulminelli, J. Molitoris, Phys. Rep. **243**, 1 (1994).
[20] Y. Abe, S. Ayik, P.G. Reinhard, E. Suraud, Phys. Rep. **275**, 49 (1996).
[21] P.-G. Reinhard, A.S. Umar, K.T.R. Davies, M.R. Strayer, and S.-J. Lee, Phys. Rev. C **37**, 1026 (1988).
[22] J.A. Maruhn, P.-G. Reinhard, P.D. Stevenson, and M.R. Strayer, Phys. Rev. C, **74**, 027601 (2006).
[23] W. J. Swiatecki, Proc. Int. School-Seminar on Reactions of Heavy Ions with Nuclei and Synthesis of New Elements, Dubna, 1975 (JINR-D7-9734).
[24] J. A. Maruhn, Proc. Topical Conf. on Heavy-ion collisions, Oak Ridge National Laboratory report CONF-

- 770602, Fall Creek Falls State Park, TN (1977).
- [25] J. Blocki, Y. Boneh, J. R. Nix, J. Randrup, M. Robel, A. J. Sierk, and W. J. Swiatecki, *Ann. Phys.* **113**, 330 (1978).
- [26] J. Randrup and W. Swiatecki, *Ann. Phys. (N.Y.)* **125**, 193 (1980).
- [27] J. Randrup and W. J. Swiatecki, *Nucl. Phys.* **A429**, 105 (1984).
- [28] J. A. Maruhn, "Invited paper presented at International Symposium of Deep Inelastic Reactions and Fusion with Heavy Ions", Berlin, (1979).
- [29] A. J. Sierk, S. E. Koonin, and J. R. Nix, *Phys. Rev.* **C17**, 646 (1978).
- [30] S. E. Koonin and J. Randrup, *Nucl. Phys.* **A289**, 475 (1977).
- [31] E. P. Wigner, *Phys. Rev.* **40**, 749 (1932).
- [32] M. Brack and R. K. Bhaduri, *Semiclassical Physics*, (Addison-Wesley, Reading 1997).
- [33] P. L'Eplattenier, E. Suraud, P.G. Reinhard, *Ann. Phys. (NY)* **224**, 426 (1995).
- [34] A. A. Vlasov, "Many-Particle Theory and Its Application to Plasma", Gordon and Breach, New York (1961).
- [35] K. Takahashi, *Prog. Theor. Phys. Suppl.* **98**, 109 (1989)
- [36] F. Toscano, A. M. Ozorio de Almeida, *J. Phys. A* **32**, (1999)
- [37] H. Krivine, J. Treiner, and O. Bohigas, *Nucl. Phys. A* **336**, 155 (1980).
- [38] F. Calvayrac et al, *Phys. Rep.* **337** (2000) 493.
- [39] M. Bender, P.-H. Heenen, and P.-G. Reinhard, *Rev. Mod. Phys.* **75**, 121 (2003).
- [40] V. Blum, G. Lauritsch, J. A. Maruhn, and P.-G. Reinhard, *J. Comput. Phys.* **100**, 364 (1992).
- [41] P.-G. Reinhard and R. Y. Cusson, *Nucl. Phys.* **A378**, 418 (1982).
- [42] H. Flocard, S. E. Koonin, and M. S. Weiss, *Phys. Rev.* **C17** (1978) 1682-1699.
- [43] P. -G. Reinhard and H. Flocard, *Nucl. Phys.* **A584**, 467-488 (1995).
- [44] V. E. Oberacker, A. S. Umar, J. A. Maruhn, and P.-G. Reinhard *Phys. Rev. C* **82**, 034603 (2010)
- [45] R. Balescu, *Equilibrium and Non-Equilibrium Statistical Mechanics* (Wiley, New York, 1975).
- [46] R. Y. Cusson, P.-G. Reinhard , J. A. Maruhn, W. Greiner, and M. R. Strayer, *Z. Phys. A* **320**, 475 (1985).
- [47] A. S. Umar and V. E. Oberacker, *Phys. Rev. C* **73**, 054607 (2006).
- [48] M. Brack , *Rev. Mod. Phys.* **65**, 677 (1993).